3D surface properties of glacier penitentes over an ablation season, measured using a Microsoft Xbox Kinect.

Lindsey. I. Nicholson[1], Michał. Pętlicki[2,3], Ben. Partan[4], and Shelley. MacDonell[3]

[1] *Institute of Atmospheric and Cryospheric Sciences, University of Innsbruck, Innsbruck, Austria*
[2] *Institute of Geophysics, Polish Academy of Sciences, ul. Księcia Janusza 64, 01-452 Warsaw, Poland*
[3] *Centro de Estudios Avanzados en Zonas Áridas (CEAZA), La Serena, Chile*
[4] *University of Maine, Orono, USA*

Correspondence to: L. I. Nicholson (lindsey.nicholson@uibk.ac.at)

Abstract. In this study, the first small-scale digital surface models (DSMs) of natural penitentes on a glacier surface were produced using a Microsoft Xbox Kinect sensor on Tapado Glacier, Chile (30°08'S; 69°55'W). The surfaces produced by the complete processing chain were within the uncertainty of standard terrestrial laser scanning techniques. The three-dimensional positional error of alignment between the digital surface and ground control points, was on average 0.08m, but in one case reached 0.3 m, due to poor overlap of individual scanned sections comprising the surface. Between November 2013 and January 2014 penitentes become fewer, wider, deeper, and the distribution of surface slope angles becomes more skewed to steep faces. Surface lowering during this core ablation season was in the order of 0.04m day^{-1}. While morphological changes cannot be captured by manual point measurements, a key finding is that mean surface lowering is well captured by manual measurements of penitente surface height at a minimum density of 5 m^{-1} over a 5 m transverse profile. Roughness was computed by applying two previously published geometrical formulae; one applied to the 3D surface and one to single profiles sampled from the surface. Morphometric analysis shows that skimming flow is persistent over penitentes, providing conditions conducive for the development of a distinct microclimate within the penitente troughs. Numerous options for representative roughness element height were used, and the calculations were done both with and without application of a zero displacement height offset to account for the likelihood of skimming air flow over the closely-spaced penitentes. Calculated roughness values are in the order of 0.01-0.10 m during the early part of the ablation season, increasing to 0.10-0.50 m after the end of December, in line with the largest previously published surface roughness values for glacier ice. Calculated surface roughness is strongly dependent on wind direction. For values calculated from 3D surfaces maximum roughness coincides with airflow across the penitente lineation while maximum roughness computed from sampled profiles coincides with airflow along the penitente lineation. These findings highlight the importance of determining directional roughness and wind direction for

strongly aligned surface features and also suggest more work is required to determine appropriate geometrical roughness formulae for linearized features.

1. Introduction

Penitentes are spikes of snow or ice, ranging from a few centimetres up to several metres in height that can form during the ablation season on snowfields and glaciers. They are a common feature of high elevation, low-latitude glaciers and snowfields (e.g. Hastenrath and Koci, 1981; Corripio and Purves, 2005; Winkler et al., 2009) where very low humidity, persistently cold temperatures and sustained high solar radiation favour their development (Lliboutry, 1954). As cryospheric water resources are relatively important to local dry season water supply in arid mountain ranges (Kaser et al., 2010), there is potential value in understanding how penitentes might influence both runoff and atmospheric humidity.

Penitentes form linearized, inclined fins of snow or ice on the surface. Both the latitudinal range (within 55° of the equator on horizontal surfaces) and geometry (aligned with the arc of the sun across the sky, and tilted toward the sun at local noon) of penitentes are governed by solar-to-surface geometry (Lliboutry, 1954; Hastenrath and Koci, 1981; Bergeron et al., 2006; Cathles et al., 2014). During the initial stages of penitente development, ablation is thought to proceed by sublimation alone, driven by low atmospheric humidity. Surface irregularities focus reflected solar radiation within depressions (Amstutz, 1958; Corripio and Purves, 2005; Lhermitte et al., 2014; Claudin et al., 2015) such that the energy receipts, and consequently ablation, are enhanced in the hollow and the surface irregularity becomes amplified. Subsequently, as the surface relief increases, a more humid microclimate can develop in the hollows between penitentes, supressing sublimation and thereby allowing melting in the depressions. The penitentes tips continue to ablate by sublimation alone (Lliboutry, 1954; Drewry, 1970; Claudin et al., 2015) and, as melting requires approximately an eighth of the energy of sublimation to remove the same amount of ice, the spatial differentiation of ablation processes between penitente trough and tip amplifies the penitente surface relief.

The altered partitioning of ablation between sublimation and melting in penitente fields, as compared to surfaces without penitentes (e.g. Lliboutry, 1998; Winkler et al., 2009; Sinclair and MacDonell, 2016), is expected to alter the rate of mass loss and meltwater production of snow and icefields during the ablation season, but this has not yet been fully quantified (MacDonell et al., 2013). Previous studies, based on radiative modelling within idealized penitente surfaces, have investigated the impact of penitentes on the shortwave radiative balance (Corripio and Purves, 2005; Cathles et al., 2014; Lhermitte et al., 2014). The results suggest that penitentes reduce effective albedo by up to 40% compared to flat surfaces and that both shape and penitente size impact the apparent albedo as measured by ground and satellite sensors (Lhermitte, et el., 2014). The development of penitentes also manifestly alters the surface roughness properties, but neither the impact of penitentes on surface roughness, nor the associated impact on turbulent energy fluxes has been investigated. While penitentes are a relatively rare form of linearized surface feature, linear crevasses are widespread, and penitentes offer a unique test bed for investigating the significance of linearized features on effective surface roughness for various wind directions.

Determining effective surface roughness on penitente-covered surfaces is complicated, as they present very closely spaced locally high relief surfaces. This means that calculating the aerodynamic roughness length (z_0) is based not only on the absolute depth of the penitentes, but also on a zero-plane displacement (z_d), which essentially means that the base of the eddy entering the penitente field is above the depth of the penitente trough. In addition, due to the irregularity of a penitente field, a roughness sub-layer can form and interact with the upper eddy system, therein creating a complex, chaotic flow. Closely packed roughness element generally experience a wake interference regime, and in the most densely packed arrays of roughness elements skimming flow occurs (Grimmond and Oke, 1999). At the top of the roughness sublayer individual wakes caused by surface obstacles are smeared out and the flow is independent of horizontal position, and thus, observations at this level represent the integrated surface rather than individual surface obstacles. This level is known as the blending height (z_r). All these properties are dependent on the size and arrangement of surface roughness elements.

Measurements of natural penitentes required to examine their morphometry and roughness are rare (e.g. Naruse and Leiva, 1997), and difficult to obtain because the complex, and partially overhanging, surface prevents the use of simplified automated tools such as photogrammetric determination of surface profile heights (e.g. Fassnacht et al., 2009; Manninen et al., 2012) or line-of-sight surveying from fixed positions. Recent advances in close-range, mobile, depth-of-field sensors and efficient feature tacking software used in interactive computer gaming offer potentially useful tools that can be applied to resolve such problems in earth science (e.g. Mankoff and Russo, 2013). In this study a Microsoft Xbox Kinect sensor is used as a close-range mobile distance ranger to produce a series of small-scale digital surface models (DSMs). The method of DSM generation is evaluated against standard terrestrial laser scanning, and the Kinect-derived DSMs of the penitentes are used to (i) perform the first detailed examination of the morphometry of natural penitentes over the course of an ablation season; (ii) compare the volume change computed from DSM differencing with estimates based on manual measurements of surface lowering and (iii) examine the geometrical roughness properties of the sampled penitente surfaces.

2. Methods

2.1 Description of field area and measurement setup

Tapado Glacier (30°08'S; 69°55'W), which is known to develop penitentes every summer, lies in the upper Elqui Valley of the semi-arid Andes of the Coquimbo Region of Chile (Fig 1). Interannual climate variability is controlled by the El Niño Southern Oscillation (ENSO), such that during El Niño events, higher precipitation and warmer conditions are experienced (Escobar and Aceituno, 1998). Most precipitation is received during the winter (Vuille and Ammann, 1997), however convective storms can cause small precipitation events in the period from December to March (Schotterer et al., 2003). Although the glacier mass balance in the area is highly sensitive to precipitation, warming at elevation over the last 40 years has produced a rise of the glacier equilibrium line altitude of over 120 m (Carrasco et al., 2008). Annual mean temperature is below freezing and annual mean relative humidity is below 30% (Ginot et al., 1999). The glacier experiences year-round ablation by sublimation, however, melt is only produced during the summer (Sinclair and MacDonell, 2016).

Two measurement sites were analysed: the 'test site' and the 'glacier site' (Fig. 1). The 'test site' was established at a patch of snow penitentes (0.5 – 1.0 m height) within a dry stream bed at 4243 m a.s.l. in the glacier foreland (Fig 1). This site was used to (i) test instrumental setups to optimize the field operation of the Kinect sensor, and (ii) compare the performance of the Kinect sensor against a Terrestrial Laser Scanner (TLS). It was chosen to avoid the logistical difficulties of transporting the TLS to the glacier. Subsequently, two study plots were established at the 'glacier site' at an elevation of 4774 m a.s.l. in the glacier ablation zone (Fig 1). These sites were scanned repeatedly with the Xbox Kinect (see section 2.3) during the core ablation season between the end of November 2013 and the beginning of January 2014. The location and layout of the two glacier plots are shown in Fig 1a. Site A (5 m by 2 m) was measured four times, on 25 November, 11 December, 20 December and 3 January. Site B (2 m by 2 m) was only measured on the last three dates. The corners of the study sites were marked with 2 m lengths of plastic plumbing piping hammered vertically into the snow, or drilled into the ice (Fig 1c). The positions of these stakes were measured using a Trimble 5700 differential GPS with Zephyr antenna on the 25th November to provide ground control points and a common reference for each survey. On each visit to the glacier, when possible, the stakes were hammered further into the snow and the resultant lowering of the stake top was noted. The maximum standard deviations of the GPS stake positions were < 1.0 cm, 1.1 cm and 1.7 cm in easting, northing and elevation respectively, with combined XYZ standard deviation < 2.0 cm for all stakes (Supplement A). Error on the manual measurements of height offsets of the marker stakes on subsequent survey dates is conservatively estimated to be 2.0 cm. This results in total positional errors of the ground control points at each scan date of between 2.3 and 2.7 cm depending on the stake. Manual measurements of surface lowering were made along the eastern long side of site A. All surfaces heights were referenced to the elevation of the glacier surface at the upglacier end of this cross profile at the date of installation.

An automatic weather station (AWS) on a free-standing tripod was installed beside the two glacier plots to provide meteorological context for the measurements, as well as an independent measure of local surface lowering (Fig 1). The sensors installed, and variables recorded, are detailed in Table 2. During the study period one significant snowfall event occurred on the 8^{th} December 2013, when the sonic distance ranger recorded a surface height increase of 0.09 m over the course of the day (Table 2).

2.2 Terrestrial laser scanning

At the 'test site', surface scans produced by the Kinect sensor were compared with those produced by well-established TLS methods. An Optech ILRIS long-range terrestrial laser scanner was used as it is especially suitable for surveying snow and ice surfaces due to having a shorter wavelength laser beam (1064 nm) than other models. This equipment surveys surface topography based on time-of-flight measurement of a pulsed laser beam reflected to a given angle by a system of two rotating mirrors. It has a raw range accuracy of 4 mm at 100 m distance, raw angular accuracy of 80 µrad, beam diameter of 27 mm at 100 m distance and beam divergence of 250 µrad. The instrument was placed in five locations around the surveyed snow patch and boulder, overlooking it from different directions. Positions of the TLS were measured with Trimble 5700 differential GPS with Zephyr antennae in static mode. Seventeen point clouds were obtained with nominal resolution of 0.11-0.75 cm. Resulting point clouds were corrected for atmospheric pressure, temperature and humidity using data from a weather station in the glacier forefield, and then trimmed using ILRIS Parser software, aligned with Polyworks IMAlign software into a common local coordinate system and georeferenced with differential GPS measurements using Polyworks IMInspect software. The alignment error of the point clouds as estimated by this software is 0.36-0.87 cm and comparison with ground control points gives an error of 5.65 cm. The TLS scan of the snow penitentes is presented as an example of the nature of the DSM that can be obtained within a penitente field using TLS (Fig 2). Due to logistical constraints, the scans of snow penitentes could not be carried out with both the TLS and Kinect on the same day, so direct comparison of the TLS and Kinect scans is instead performed on a reference boulder within the test site, whose surface is assumed unchanged between different scan dates.

2.3 Kinect surface scanning

The Kinect sensor emits a repeated pattern of structured infra-red (IR) beams, and records the pattern distortion with an IR camera. The depth-of-field calculation is performed via a proprietary algorithm and a distance map is the raw data output. Using the standard calibration the static raw depth field resolution of the Kinect is 1 mm and the distance error is < 1.0 cm at the distance range of the penitente scans (Mankoff and Russo, 2013).

For its original gaming usage, the Kinect is in a fixed position and proprietary software uses feature tracking to monitor movements of players within the field of view of the Kinect. The inverse of this workflow can also be applied whereby the Kinect sensor is moved interactively around a static surface or 3D body, using the same feature tracking to compute the position of the sensor relative to the object and thereby allowing a point cloud reconstruction of the object. In this work we apply the second work flow and sample Kinect data using ReconstructMe™ 2.0 software. In common with alternative reconstruction packages compatible with the Kinect, ReconstructMe™ performs bilateral filtering on the output depth map frame and converts the pixel version of each depth map frame to 3D coordinate maps of vertices and normals. An iterative closest point (ICP) alignment algorithm is then applied frame by frame at three scales to repeatedly rotate and translate the depth field to determine camera position and an aligned surface, giving weighted preference to portions of the surface that are perpendicular to the line of sight. The ReconstructMe™ software has the advantage of producing surface meshes in real-time, so that the operator can check the scan quality and coverage at the time of capture, but the disadvantage that the raw point cloud is not saved and if the real-time tracking is lost a new scan must be started.

The Xbox Kinect was connected via a 5m powered USB extension cord to an MSI GE60 gaming laptop, powered using a 240V 600W inverter connected to the 160Ah 12V battery of the automatic weather station on the glacier. Scans were carried out by two people; one handling the Kinect and the other monitoring the quality of the surface being generated. In bright conditions, the return IR signal of the Kinect is swamped by natural radiation over snow and ice surfaces, which reflect a high proportion of incident shortwave radiation, and absorb or scatter much of the longwave radiation signal. Therefore, scanning was carried out at twilight or just after nightfall. Sudden movements caused by the operator slipping or the snow compacting underfoot resulted in loss of tracking of common reference points. Consequently, each study site was scanned in small sections and three to thirteen overlapping surface meshes were used to cover the area of each study site.

2.4 Kinect surface mesh processing

The full mesh processing procedure using the freely-available Meshlab software is presented in Supplement B, and briefly described here. Small surface components, unreferenced and duplicated vertices were removed from the meshes using inbuilt filters. The component meshes that cover each sampling date at a single site were aligned using an iterative closest point (ICP) algorithm which distributes the alignment error evenly across the resultant mosaicked surface mesh. Alignment solutions consistently had mean distributed error < 4 mm (Supplement B). The aligned meshes were flattened into a single layer, remeshed using a Poisson filter and resampled to reduce the point density by setting a minimum vertex spacing of 2.5 mm.

The surface mesh for each scan date was georeferenced in Polyworks software using the known coordinates of the base of the marker stakes at the time of each scan because the upper portions of the symmetrical stakes are often poorly captured by the meshing software. The local elevation zero was set to be the north-east corner of site A. The mismatch evident in the georeferencing step (Table 1) is much larger than the mesh alignment error (Supplement B). This is most likely an artifact of a combination of (i) reduced mesh quality at the margins of the component scans and (ii) insufficient overlap between some scan sections producing distortion within the mesh alignment.

To eliminate the marker stakes and any data gaps near the margins of the study areas, each surface mesh was sub-sampled within the staked area. The sub-sampled area for site A is a 2.0 by 3.5 m horizontal area (7.00 m^2), and site B is a 1.5 m x 1.5 m horizontal area (2.25 m^2) shown in the examples in Figure 3. Mesh vertices and an index file of the vertices comprising each face were exported from Meshlab for subsequent analysis in Matlab software.

2.5 Calculations of surface geometrical properties

The geo2d and geo3d toolboxes (available from the Matlab File Exchange) were used to compute the face areas and normals of the mesh, from which surface height distribution, aspect and dip of the sampled surface were calculated, weighted by the ratio of each face area to the total surface area of all faces. As the surfaces contain overhanging parts, DSM differencing cannot be performed by simple subtraction. Instead surface lowering was calculated in two ways: Firstly by differencing area-weighted mean surface elevations, and secondly by computing the volume change between scan dates. For the latter approach, volumes for all surfaces were computed relative to a baselevel horizontal reference. Volumes relative to this horizontal reference for upward-facing triangles were computed column-wise, by projecting the area of each triangular face onto the reference surface and using the height coordinate of the triangle centroid as the height dimension for each column. These were summed and volumes for overhanging triangles, calculated in the same way, were subtracted to derive the total volume between the reference surface and each scanned penitente surface. Successive volumes were then subtracted to obtain the volume change over each measurement interval. The volume-differencing approach is expected to be the more accurate of the two methods as it accounts for over-hanging surfaces.

2.6 Manual measurements of surface change

Traditional single-point stake measurements of glacier surface lowering are unreliable within the inhomogeneous surface of a penitente field. One alternative is to measure surface lowering at intervals along a profile perpendicular to the main axis of alignment of the penitentes. Such a reference was installed along the 5 m-long eastern margin of site A, between two longer corner stakes drilled 3 m into the ice using a Kovacs hand drill. The distance between a levelled string and the glacier surface was measured using a standard tape measure at 0.2 m intervals on 23 November. Subsequent measurements, on the 12 and 21 December and on 4 January, were made at 0.1 m intervals. All measurements were recorded to the nearest centimetre, and the error on each measurement is estimated to be 2.0 cm, which is assumed to capture the error associated with the horizontal position of the measurements along the reference frame and the vertical measurements of the distance to the surface beneath.

2.7 Calculations of geometric surface roughness

Morphometric determinations of surface roughness have been shown to be viable, and generally more easily implemented, alternatives to aerodynamic determinations of surface roughness (e.g. Kondo and Yamazawa, 1986; Munro, 1989; Grimmond and Oke, 1999; Fassnacht et al., 2009; Andreas, 2011). The surface meshes created from the Kinect measurements were used to calculate *z0* using a widely-used relationship established by Lettau (1969), initially developed for isolated, regular obstacles distributed over a plane:

$$z_0 = 0.5\, h \left(\frac{s}{S}\right) \qquad (1)$$

where h is the height of the obstacles, s is the upwind silhouette area of each obstacle and S is the specific area occupied by each roughness element obstacle, also referred to as its lot area. Following Macdonald and others (1998), h was replaced by average obstacle height, s with the sum of all the upwind silhouette areas, and S with the total area covered by the obstacles. While the upwind silhouette area, and indeed surface area in any direction, is relatively easily defined for each surface mesh area using trigonometry, it is difficult to define individual roughness elements and their representative heights, due to the lack of an apparent base level. Surfaces were first detrended to remove any general surface slope at the site, then roughness for the detrended 3D meshes is calculated assuming that the roughness elements cover the whole surface area (i.e S = plot area), and for four possible representations of average obstacle height (h) as follows: (i) the maximum range of the detrended mesh; (ii) twice the standard deviation of the detrended surface mesh; (iii) mean mesh height above the mesh minimum; and (iv) median mesh height above the minimum.

Penitente fields are expected to exceed the 20-30% roughness element density criterion below which Equation 1 applies (Macdonald et al., 1998). Above this limit, skimming flow is expected and .consideration of an appropriate zero displacement height is needed. As z_d is also unknown in the case of penitente fields, sample calculations of three-dimensional roughness on the detrended surface meshes were made using three possible realizations of z_d: $zd = h$; $zd = 2/3h$ (following Brutsaert, 1975); $zd = 1/3h$. Each z_d case is computed for the four values of h previously outlined. Equation 1 is then applied to the roughness elements remaining above the plane of the general surface slope offset by a distance z_d above the minimum height of the surface mesh. The representative height h for this portion of the mesh exceeding the plane is taken to be the mean area-weighted height of all triangles above this plane, s is the summed frontal area of all mesh triangles above z_d that face into the chosen wind direction and S is the total horizontal area of the surface components above z_d.

Finally, roughness was calculated for cross-sections of length X, sampled perpendicularly to the wind direction following Munro (1989, 1990). Here, h is replaced with an effective height h^* expressed as twice the standard deviation from the standardized mean profile height; s is replaced with $h^*X/2f$, in which f is the number of profile sections that are above the mean elevation; and S is replaced with $(X/f)^2$. To investigate the nature of the roughness computed this way for north-south and east-west impinging wind directions, cross profiles longer than 1.5 m at 0.1 m intervals orientated E-W and N-S were extracted from each scanned surface. Cross-sections were detrended to remove the influence of any general surface slope at the site, and roughness was computed on each of these cross-sectional profiles following the modifications of Munro. Mean profile roughness for these two wind directions are presented for each sampled surface.

3. Results

3.1 Evaluation of the quality and suitability of penitente scans by TLS and Kinect

The penitente surface produced by the TLS did capture some overhanging surfaces but only 58% of the total horizontal surveyed area was captured as the deepest parts of the troughs were obscured from the view by the surrounding penitentes (Fig 2a). In comparison, the Kinect system scanned 100% of the survey area.

For the direct comparison of the two methods on a reference boulder, the Kinect-derived surface, produced from three mosaicked meshes was aligned to the surface produced from the TLS point clouds. The TLS scan was incomplete, with parts of the top and overhanging surfaces of the boulder missing due to being obscured from the TLS survey positions, while the Kinect scan achieved complete coverage of the boulder. The difference between the two aligned meshes where overlapping data existed was always < 2 cm, which is well within the uncertainty of the georeferenced TLS surface model. Larger differences of up to 5 cm, evident in Figure 2b, occur only where there are data gaps in the TLS surface being compared.

It is difficult to formally assess the total error of the surfaces produced by the Kinect scans because the workflow involves several black box processing steps. The mean alignment errors of the mesh mosaicking step in Meshlab is < 0.4 cm and quantifiable errors associated with the GPS positions, subsequent measurement of the stake bottom positions relative to the GPS positions are all < 2.0 cm. However, the three-dimensional georeferencing error in this study is large (Table 1) compared to the other sources and is therefore taken as a reasonable value for the uncertainty of the total process chain. Errors given on the seasonal mass, volume and surface changes are based on summing the squares of the mean elevation difference between the marker stakes and ground control points (GPCs) at each site on the first and last survey dates.

3.2 Morphometric changes and surface lowering

The morphometry of the sampled penitentes changed visibly over the measured intervals (Figs 3 and 4). The strong east-west lineation and preferred north and south surface aspect predicted from theory developed early and were maintained throughout study period. Over time penitente troughs became fewer in number, but wider and deeper. This causes total surface area to increase; at site A the true surface is between 1.7 and 4.0 times the horizontal equivalent area, and at site B between 2.1 and 3.7 times the horizontal surface area equivalent (Fig 4 a & b). Snowfall during the first measurement interval decreases the surface area at site A over that interval. Surface relief, expressed by the vertical range of the mesh, also increases through time, except when snowfall partially filled the developing penitentes and reduces both the range of the surface and the general slope angle. The largest part of the surface is facing southwards, and the predominant angle generally steepens over time, though again this trend is reversed by snowfall (Fig 4 c & d). From the onset of measurements the surface aspect distribution is strongly dominated by north and south facing components and this becomes more pronounced in the latter measurements and the preferred orientation rotates slightly over the course of the season (Fig 4 e & f).

Surface lowering rates derived from calculated volume changes per unit area were 21, 41 and 70 mm d^{-1} over each interval at site A, and 57 and 61 mm d^{-1} over the last two intervals at site B. In comparison, surface lowering rates calculated from area-weighted mean mesh elevation were within a few millimetres of those derived from volume changes: 22, 38 and 69 mm d^{-1} for the three measured intervals at site A, and 54 and 60 mm d^{-1} for the last two intervals at site B. The increasing rate of surface lowering through time is associated with progressively increasing atmospheric energy supply and surface properties becoming more conducive to melting. The warming atmosphere is expressed in the positive degree days of the three periods which are 3.7, 2.2 and 31.5 over the 16, 9 and 14 day-long periods respectively.

Total surface lowering over the whole available data period for each site computed by volume change (area-weighted mean height change) was 1.68 (1.77) ± 0.11 m at site A and 1.37 (1.32) ± 0.38 m at site B. Over the common measurement period, surface lowering at site A was 1.35 (1.31) ± 0.21 m, indicating that lowering rate is repeatable at both sites. Volume loss was converted to mass loss using the mean snow density of 426 kg m^{-3} (with an assumed uncertainty of ± 5%) measured in a 1.10 m snow pit excavated on 22 November 2013 beside the AWS. Mass loss at site A computed from mesh volume change (area-weighted height change) between 25 November and 3 January was 716 ± 58 (754 ± 59) kg m^{-2}. Mass loss at site B from mesh volume changes (area-weighted height changes) between 11 December and 3 January was 582 (562) ± 166 kg m^{-2}. Measurements at site A over the same period give mass loss of 573 (558) ± 95 kg m^{-2}, so again, measurements at both sites are within the range of uncertainty.

3.3 Manual measurements of reference cross-profile

Intermittent measurements cross-cutting the predominant penitente alignment do not capture the complexity of the surface as revealed by the Kinect surface sampling (Fig 5). Over the 39 days of the study, the mean mass loss calculated from 26 points spaced at 0.2 m intervals along a 5 m profile crosscutting the penitentes at site A was 1.61 ± 0.14 m, which equates to a mass loss over the same period of 688 ± 70 kg m^{-2}. This differs from the value calculated from volume change computed from surface meshes consisting of over 1.3 million points and covering an area of 7 m^2 by only 28 kg m^{-2}, which is within the uncertainty of the two measurement methods. Assuming that this difference holds true for the whole ablation season of 120 days, point measurements underestimate the seasonal mass loss obtained from the Kinect digital surface models by 86 kg m^{-2}.

To investigate the impact of sampling resolution on the manual measurements and how the derived surface lowering compares to the Kinect-derived lowering, maximum elevation range, mean surface height (compared to the horizontal reference) and mean surface lowering, were calculated from manual measurements at 0.1 (n = 52), 0.2 (n = 26), 0.4 (n = 14) and 1.0 m (n = 6) intervals on the last three measurement dates. The highest resolution sample was taken as a reference against which to evaluate coarser sampling. Surface relief differed from that measured at 0.1 m by maxima of 0.13, 0.29 and 0.41 m for 0.2, 0.4 and 1.0 m sampling intervals respectively. Mean measured surface height was within 0.03 m of the highest resolution measurements at 0.2 m and 0.4 m intervals, and within 0.12 m at 1.0 m resolution. Mean lowering rates at 0.1, 0.2 and 0.4 m sampling intervals were all within 3 mm d^{-1}. This increased to a maximum of 12 mm d^{-1} when the sampling resolution was decreased to 1.0 m. Decreasing the length of the sampled profile down to 2 m alters the mean lowering rate by less than 5 mm d^{-1} at sampling resolutions of 0.1, 0.2 and 0.4 m.

Probing of the snow along the line of the horizontal reference on 25 November indicated mean snow depth of 1.83 m (standard deviation 0.56 m). The underlying ice surface does not appear to be influencing the structure of the overlying snow penitentes (Fig 5). However, it is difficult to draw a firm conclusion based on these measurements, particularly as, while the surface of the penitentes was still snow on the 3 January, in several instances the surface had lowered below the level of the ice interface suggested by the initial probing. This highlights the difficulty in identifying the underlying ice surface, or summer ablation surface, within a penitente field, suggesting that a single location must be sampled very densely to obtain a characteristic snow depth by this method.

3.4 Surface roughness assessments

The representative height, *h*, used in the calculations increases over time in all cases, and is bounded by the maximum (*h* as range of the detrended surfaces), and minimum (*h* as twice the standard deviation of the detrended surface) cases (Fig 6). Differences in *h* computed by the same method can reach as much as 0.2 m between the two sites, although the pattern of change over time is consistent.

The application of Lettau's (1969) formula is considered to be invalid if the ratio of the frontal area to the planar area of the obstacles exceeds 20-30%, implying skimming airflow. .This ratio is greater than 20% for all of the penitente surfaces, and after the 20th December is always greater than 30%. If this issue is ignored, calculated z_0 values increase with time and show a strong dependence on the impinging wind direction, with values peaking for wind directions perpendicular to the alignment of the penitentes (Fig 7). Calculated z_0 ranges from 0.01 – 0.90 m, depending on the way in which the representative height is expressed, the date and the wind direction (Fig 8). Given the close spacing of the penitentes it is likely to be more valid to explore what z_0 would be when a zero displacement height offset is applied. Introducing the zero displacement height reduces the maximum calculated roughness by about half, and also reduces the variability between different representative heights (Fig 8), as a smaller *h* value translates into a smaller z_d so that the calculation is performed on a larger portion of the mesh.

Surface roughness assessments on the basis of calculations following Munro's modification for single profile measurements were applied to cross profiles longer than 1.5 m at site A (B) yielding 20 (6) profiles orientated N-S and 33 (7) E-W. Surface amplitude increases over time, and the amplitude of the N-S running cross profiles is generally larger than the E-W running cross profiles, as illustrated in the example of site B (Fig 9). Table 3 shows the calculated roughness values at each survey date, revealing that while profile-computed roughness length increases monotonically over time at site B, it reduces over the first period at site A, associated with snowfall during this period. Both the range and relative increase in roughness over time is larger for the N-S running profiles. The computed roughness at both sites is 4.3 to 6.8 times larger for airflow impinging on the penitente field in an E-W direction than for airflow in the N-S direction. This is contrary to the results computed on the full 3D mesh surface, but is understandable because this formulation relies on the amplitude of the surface, which is generally larger in the N-S orientated cross profiles than the E-W running cross profiles.

Prevailing wind direction differs only slightly in each period with an increasing northwesterly component in the second two periods compared to the first. This may be related to the occurrence of snow during the first period, which is expected to alter thermally-driven valley wind systems. Over the whole study period wind direction is predominantly from the south-easterly and north-westerly sectors, and swings through both extreme wind angles used in the roughness calculations here (Fig 10). This indicates that the effective roughness at this site can be expected to differ significantly over time depending on the wind direction.

4. Discussion

4.1 Methods of measuring change of rough glacier surface elements

The test site for scanning penitentes with a TLS was chosen as scanning positions could be established on the surrounding higher ground overlooking the penitente field, thereby offering the best viewing angles possible. Nevertheless, the terrestrial laser scanning could only capture the upper portions of the penitentes. As ablation is at its maximum in the troughs, TLS data cannot capture the true volume change of penitentes. In contrast, the Kinect sensor can be moved across the complex relief of the penitente field to make a complete surface model. Although it is in principle possible to capture a large area with the ReconstructMe software used here, and it offers the advantage of providing real time feedback on the mesh coverage, it proved difficult to capture the study sites in a single scan given (i) the reduced signal range of the sensor over snow and ice (Mankoff and Russo, 2013), and (ii) the difficulty of moving around the penitente field. As a result, partial scans were obtained, with the disadvantage that subsequently combining these introduces a substantial degree of additional error associated with alignment if the component scans were not of high quality at the margins, or did not overlap adjacent scan areas sufficiently. The practical utility of the Kinect on glacier surfaces is limited to small study areas, but integrating local findings with glacier wide TLS or photogrammetric information of surface conditions may offer a means to usefully extrapolate small scale findings to the glacier scale. Surface scanning technology and software is an area of rapid development, and ongoing development of new sensors and airborne platforms may eliminate the challenges of producing high quality depth maps over larger areas using similar technology to the Kinect.

Despite not visually capturing the complex morphology of the penitentes, manual measurements of surface height change in a penitente field along a profile cross-cutting the penitentes are found to be robust for determining mean surface lowering rates, and show good agreement to the volume changes computed from differencing the digital surface models scanned in detail using a Kinect. Comparison of the manual sampling at different intervals suggests that five samples per meter is adequate to characterize surface change of penitentes, but that data will be unreliable is the cross-profile is too short.

4.2 Penitente morphology

Although the penitentes sampled here are more convoluted than the parallel rows of penitentes used in model representations (Corripio and Purves, 2005; Lhermitte et al., 2014), the morphometric properties of the meshes are similar to the morphometric properties of simplified surfaces. The penitente surface represents a much larger total surface area than the equivalent non-penitente surface and the control of solar radiation on penitente morphology (Cathles et al., 2014) means that the vast majority of the surface consistently dips steeply to the north and south at all stages of development.

Unless a snowfall event occurs to partially fill the troughs, surface relief, slope angle, penitente spacing and total surface area all increase over time as the penitentes develop. Thus the impact of penitentes on surface properties will also change along with the morphological changes. At Tapado Glacier, penitentes are initially overhanging to the north, and the southfacing sides are convex compared to the northfacing overhanging faces. Over the season the penitentes become more upright as the noon solar angle gets higher, and these changes in morphology may in turn alter the effect of the penitentes on surface albedo (Lhermitte, et al., 2014). In the context of the numerical theory of Claudin and others (2015), penitente spacing controls the atmospheric level at which water vapor content is representative of the bulk surface properties. Simultaneous field or laboratory measurements of penitente spacing evolution and vapor fluxes above the surface would be required to confirm this, but the spacing from the field measurements provided here can be used as an indication of the level at which measurements would need to be made in order to capture the bulk surface fluxes rather than fluctuations governed by the small-scale surface terrain.

4.3 Surface roughness

Given that aerodynamic measurements to determine the most suitable representative height and zero displacement level for penitentes are thus far unavailable, the approach taken here was to do an exploratory study and compute geometric surface roughness values using various ways of expressing *h* and z_d. As a consequence the results are purely illustrative and while patterns can be drawn from them that have meaning for understanding the nature of the computation, the applicability of these values in turbulent exchange calculations remains to be established.

The ratio of frontal to planar area of the penitentes implies that skimming flow prevails, such that turbulent airflow in the overlying atmosphere does not penetrate penitente troughs. This is in agreement with the theory of formation and growth of penitentes, in which the development and preservation of a humid microclimate within the penitente troughs is required to facilitate differential ablation between the trough and tip of the penitente. Although the data here shows that penitentes become less densely packed over time, skimming flow regime persists over the study period, and available data is insufficient to determine if this holds true to the end of the ablation season.

The changing morphometry of the penitentes alters the geometrical surface roughness as they develop over the ablation season. Roughness calculated using a range of possible representations of *h* and $z_d$give roughness values in the order of 0.01-0.10 m during the early part of the ablation season and 0.10-0.50 m after the end of December. These values are in line with values previously published for rough glacier ice (Smeets et al., 1999; Obleitner, 2000). This roughness increase is related to the deepening of the penitentes over time and an increase of the surface amplitude. Lettau's (1969) formula, which does not account for z_d, overestimates roughness for densely packed obstacles, but this does not compensate sufficiently to reproduce values of $z_d + z_0$ for densely packed obstacles from formulations that include z_d in the computation of z_0. Thus, Lettaus formula is expected to estimate the zero velocity point of a logarithmic wind profile to be lower than formulations that include z_d in the computation of z_0. The pattern of the computed roughness properties is consistent between the two neighbouring sites, but individual values can differ, suggesting that relief varies substantially over short distances and sampling a large area is necessary to capture mean properties.

The strong alignment of penitentes means that calculated roughness is strongly dependent on wind direction. Roughness calculated from 3D surface meshes are higher for wind impinging in a north-south direction, as the large faces of the penitentes form the frontal area in this case. In contrast, roughness calculated for individual profiles extracted from the mesh to mimic manual transect measurements in the field, is between 3 and 6 times larger for air flow impinging in an east-west direction, than in a north-south direction. As neither approach has been evaluated against independent surface roughness derived from atmospheric profile measurements over penitentes, the available data is insufficient to distinguish if maximum effective aerodynamic roughness is associated with wind flowing across or along the penitente lineation, and the appropriate relationship between wind direction and surface roughness for calculating turbulent fluxes over penitentes remains elusive. It principle it sounds reasonable to expect airflow across the penitente lineation to maximize turbulence as the penitentes present a large surface area to the wind, yet, if skimming flow is established, with the result that only the tips of the penitentes are determining the structure of the turbulence then effective roughness in this direction would be strongly reduced, and perhaps even be less than for air flow along the penitente lineation, for which the smaller frontal area reduces the likelihood of skimming flow. Further investigation of this in order to quantify the impact of penitentes on turbulent fluxes for various airflow patterns would require high resolution turbulence modelling or direct measurement of aerodynamic roughness and turbulent fluxes over penitentes in all wind directions.

In this study we did not explicitly compute the blending height as available formulae are dependent upon z_0 and z_d. Estimates of the blending height independently from z_0 and z_d have been suggested to be 2.5 - 4.5 times h, as twice the mean element spacing, or as combination of the height and spacing (see examples within Grimmond and Oke, 1999). Given that only atmospheric measurements above the blending height give representations of integrated surface fluxes and conditions, the first approach would imply that aerodynamical or flux measurements over penitentes would have to be carried out at considerable height above the surface to capture mean surface properties rather than the effects of individual roughness elements. The mathematical model of Claudin and others (2015) gives a characteristic length scale for the level at which the vapour flux is constant in horizontal space that is related to the spacing of the penitentes. Interpreting this level as the blending height implies that the blending height might be determined on the basis of spacing of penitentes alone, and that this in turn might contain useful data for understanding the structure and efficiency of turbulence above penitentes. Exploring these ideas requires information from detailed meteorological measurements as well as the geometrical information offered in this paper.

5. Conclusion

This study demonstrates that the Microsoft Kinect sensor be used successfully at close range over rough snow and ice surfaces under low light conditions, to generate small-scale digital surface models useful for assessing morphometry and surface roughness properties of complex terrain, as well as detailed assessments of spatial variability of surface ablation. The data collected in this study offers the first detailed study of how the geometry of penitentes evolve through time, highlighting the rate of change of surface properties over an ablation season that can serve as a guideline for parameterizing surface properties required for energy and mass balance modelling of penitente surfaces. The method demonstrated here could be useful for investigating glacier surface features such as sastrugi, crevasses or meltwater streams and determining the patterns of surface change associated with such features.

Relatively crude manual measurements of penitente surface lowering are shown to be adequate for quantifying the seasonal mass loss, which is good news for the validity of existing measurements of surface change on glaciers with penitentes. However, further measurements and/or modelling studies are required to determine if the mass loss from the expanded and convoluted surface of penitentes is enhanced or inhibited compared to mass loss in the absence of penitentes.

Aerodynamical roughness properties and related metrics over very rough surfaces remain poorly quantified and both geometric and meteorological determinations of these values show a wide spread; consequently it remains unclear what the best methods to use are or what values modellers would be best to use (Grimmond and Oke, 1999). In this context further study of penitentes offers a useful opportunity as (a) their morphometric evolution over time allows various geometries to be evaluated by monitoring a single site, and (b) they offer a bridge between wind tunnel and urban field experimentation of turbulence and roughness over extreme terrain. Although validity of surface roughness calculations based on surface geometry remains to be established for penitentes, this study highlights that (i) skimming flow is expected to persist over penitentes field, but is more likely under wind directions perpendicular to the penitente alignment; (ii) z_d is certainly greater than zero, and while the depth of penetration of surface layer turbulence into a penitente field is not clearly established it is likely to evolve with the developing penitentes, and values of $z_d \sim 2/3h$ give results that are theoretically reasonable in the framework outlined by Grimmond and Oke (1999); (iii) the two methods of geometric computation of surface roughness applied here give conflicting results as to whether the effective surface roughness of penitentes is greater for airflow along or across the penitente lineation and (iv) more complete understanding of the impact of penitentes on the turbulent structure, its evolution in time, and its directional dependency, would require atmospheric measurements with no directional bias concurrent with measurements of penitentes morphology.

Potential future applications and analyses of the surfaces generated in this study include (i) using surface properties and roughness values as a guide for input into surface energy balance models; (ii) assessing the performance of models against the measured volume loss over time and (iii) evaluating how well simplified representations of penitente surfaces used in small scale radiation models and turbulence models capture the real-world complexity. Such studies would help establish the nature of the likely micro-climatic distribution of the surface energy balance within a real penitente field, and as a result the impact of penitentes on runoff and exchange of water vapour with the atmosphere.

Author contributions. LN designed the study. Fieldwork was carried out by LN and BP with MP providing the TLS data. TLS and AWS equipment was provided by SM through collaboration with CEAZA. The data was analysed by LN and MP. Preparation of the manuscript and figures was led by LN with contributions from all co-authors.

Acknowledgements. Fieldwork for this study was funded by a National Geographic Waitt Grant awarded to L N and S M. LN was supported by an Austrian Science Fund Elise Richter Grant (V309). MP was supported within statutory activities No 3841/E-41/S/2016 of the Ministry of Science and Higher Education of Poland. International cooperation was supported by the Centre for Polar Studies from the funds of the Polish Leading National Research Centre (KNOW) in Earth Sciences (2014–18). Thanks are also due to Mathias Rotach for reading the paper prior to submission.

References

Amstutz, G. C. (1958) On the formation of snow penitentes. *Journal of Glaciology*, 3 (24), 304-311.

Andreas, E. L. (2011). A relationship between the aerodynamic and physical roughness of winter sea ice. *Quarterly Journal of the Royal Meteorological Society*, *137*(659), 1581–1588. doi:10.1002/qj.842

Bergeron, V., Berger, C., & Betterton, M. D. (2006). Controlled irradiative formation of penitentes. *Physical Review Letters*, 96(9), 098502, doi:10.1103/PhysRevLett.96.098502

Brutsaert, W. (1975). A theory for local evaporation (or heat transfer) from rough and smooth surfaces at ground level. *Water Resources Research*, 11(4), 543–550.

Carrasco JF, Osorio R, Casassa G. 2008. Secular trend of the equilibrium-line altitude on the western side of the southern Andes, derived from radiosonde and surface observations. *Journal of Glaciology,* **54**(186): 538-550, doi: 10.3189/002214308785837002.

Cathles, L. M., Abbot, D. S., & MacAyeal, D. R. (2014). Intra-surface radiative transfer limits the geographic extent of snow penitents on horizontal snowfields. *Journal of Glaciology*, 60(219), 147–154. doi:10.3189/2014JoG13J124

Claudin, P., Jarry, H., Vignoles, G., Plapp, M., & Andreotti, B. (2015). Physical processes causing the formation of penitentes. *Physical Review E*, 92(3), 033015. doi:10.1103/PhysRevE.92.033015

Corripio, J. G., & Purves, R. S. (2005). Surface energy balance of high altitude glaciers in the Central Andes: the effect of snow penitentes. In: De Jong C., Collins D.N. and Ranzi, R. (Eds) Climate and Hydrology in Mountain Areas. Wiley and Sons, Chichester, 15-27.Drewry, D. J. (1970). Snow penitents. *Weather*, 25(12), 556.

Drewry, D. J. (1970). Snow penitents. *Weather*, *25*(12), 556.

Escobar F., & Aceituno P. 1998. The ENSO phenomenon influence on snowfall in the Andean sector of central Chile during winter. *Bull. Inst. Fr. Etud. Andines* **27**(3): 753-759.

Fassnacht, S. R., Stednick, J. D., Deems, J. S., & Corrao, M. V. (2009). Metrics for assessing snow surface roughness from Digital imagery. *Water Resources Research*, 45, W00D31 doi:10.1029/2008WR006986

Ginot, P., Kull, C. Schotterer, U., Schwikowski, M. and Gäggeler, H. W. (1999) Glacier mass balance reconstruction by sublimation of chemical species on Cerro tapado (Chilean Andes). *Climate of the Past*, 2, 21-30.

Grimmond, C. S. B., & Oke, T. R. (1999). Aerodynamic Properties of Urban Areas Derived from Analysis of Surface Form. *Journal of Applied Meteorology*, 38(9), 1262–1292.

Hastenrath, S., & Koci, B. (1981). Micro-morphology of the snow surface at the Quelccaya ice cap, Peru. *Journal of Glaciology*, 27(97), 423–428.

Kaser, G., Großhauser, M., & Marzeion, B. (2010). Contribution potential of glaciers to water availability in different climate regimes. *Proceedings of the National Academy of Sciences*, 107(47), 20223–20227. doi:10.1073/pnas.1008162107

Kondo, J., & Yamazawa, H. (1986). Aerodynamic roughness over an inhomogeneous ground surface. *Boundary-Layer Meteorology*, *35*(1983), 331–348.

Lettau, H. (1969). Note on Aerodynamic Roughness-Parameter Estimation on the Basis of Roughness-Element Description. *Journal of Applied Meteorology*, 8(5), 828-832.

Lhermitte, S., Abermann, J., & Kinnard, C. (2014). Albedo over rough snow and ice surfaces. *The Cryosphere*, 8(3), 1069–1086. doi:10.5194/tc-8-1069-2014

Lliboutry, L. (1954). The origin of penitents. *Journal of Glaciology*, 2, 331–338.

Lliboutry, L. (1998). Glaciers of Chile and Argentina. In, R. S. Williams and J. G. Ferrigno (Ed). Satellite image atlas of glaciers of the world: South America. USGS Professional Paper 1386-I.

Macdonald, R. W., Griffiths, R. F. F., & Hall, D. J. J. (1998). An improved method for the estimation of surface roughness of obstacle arrays*. Atmospheric Environment*, 32(11), 1857–1864. doi:10.1016/S1352-2310(97)00403-2

MacDonell, S., Kinnard, C., Mölg, T., Nicholson, L. I., & Abermann, J. (2013). Meteorological drivers of ablation processes on a cold glacier in the semi-arid Andes of Chile. *The Cryosphere*, 7(5), 1513–1526. doi:10.5194/tc-7-1513-2013

Mankoff, K. D., & Russo, T. A. (2013). The Kinect: a low-cost, high-resolution, short-range 3D camera. *Earth Surface Processes and Landforms*, 38(9), 926–936. doi:10.1002/esp.3332

Manninen, T., Anttila, K., Karjalainen, T., & Lahtinen, P. (2012). Automatic snow surface roughness estimation using digital photos. *Journal of Glaciology*, *58*(211), 993–1007. doi:10.3189/2012JoG11J144

Munro, D. S. (1989). Surface roughness and bulk heat transfer on a glacier: comparison to eddy correlation. *Journal of Glaciology*, 35(121), 343–348.

Munro, D. S. (1990). Comparison of Melt Energy Computations and Ablatometer Measurements on Melting Ice and Snow. *Arctic, Antarctic, and Alpine Research*, 22(2), 153–162. doi:10.2307/1551300

Naruse, R. and Leiva, J. C. (1997) Preliminary study on the shape of snow penitentes at Piloto Glacier, the central Andes. *Bulletin of Glacier Research*, 15, 99-104.

Obleitner, F. (2000). The energy budget of snow and ice at Breidamerkurjökull, Vatnajökull, Iceland. *Boundary-Layer Meteorology*, 97(3), 385–410.

Schotterer U, Grosjean M, Stichler W, Ginot P, Kull C, Bonnaveira H, Francou B, Gäggeler HW, Gallaire R, Hoffman G, Pouyaud B, Ramirez E, Schwikowski M & Taupin JD. 2003. Glaciers and climate in the Andes between the equator and 30ºS: What is recorded under extreme environmental conditions? *Climatic Change,* 59(1-2), 157-175, doi:10.1023/A:1024423719288.

Sinclair, K. & MacDonell, S. (2016) Seasonal evolution of penitente geochemistry at Tapado Glacier, northern Chile. *Hydrological Processes*, 30(2), 176-186, doi: 10.1002/hyp.10531.

Smeets, C. J. P. P., Duynkerke, P., & Vugts, H. (1999). Observed wind profiles and turbulence fluxes over an ice surface with changing surface roughness. *Boundary-Layer Meteorology*, 92(1), 99–121.

Winkler, M., Juen, I., Mölg, T., Wagnon, P., Gomez, J., & Kaser, G. (2009). Measured and modelled sublimation on the tropical Glaciar Artesonraju, Peru. *The Cryosphere*, 3(1), 21–30.

Supplementary material

- A: GPS position of ground control points at each glacier site
- B: Mesh surface components and processing steps used for Kinect surface scans
- C: Kinect surface meshes for both sites on all dates as .PLY files [sX_DDMM.PLY]
- D: 3D viewer files of surfaces at site B can be seen at: https://sketchfab.com/LindseyNicholson/folders/penitentes-on-glaciar-tapado-chile

Table 1: Maximum absolute georeferencing error at each marker stake for site A and B, relative to the standard deviation of the differential GPS measurement.

	ΔX [mm]	**ΔY [mm]**	**ΔZ [mm]**	**ΔXY [mm]**	**ΔXYZ [mm]**	***dGPS XYZ standard deviation* [mm]**
A-1	63	25	38	68	77	*17*
A-2	214	118	259	233	312	*15*
A-3	14	57	53	57	62	*14*
A-4	23	29	61	33	69	*16*
A-5	54	32	128	56	139	*18*
B-1	59	46	19	75	77	*16*
B-2	121	11	102	164	193	*17*
B-3	11	48	2	49	49	*12*
B-4	85	37	34	85	92	*12*

Table 2: Mean meteorological conditions during the measurement intervals: incoming shortwave (SW in), albedo (α), incoming longwave (LW in), windspeed (u), wind direction (dir), surface temperature computed from measured outgoing longwave radiation (T surface), air temperature (T air), relative humidity (RH), air pressure (P) and the distance between the sonic ranger and the glacier surface (dist).

	SW in	**α**	**LW in**	**u**	**dir**	**T surface**	**T air**	**RH**	**P**	**dist**
	[W m^{-2}]	[-]	[W m^{-2}]	[m s^{-1}]	[°]	[°C]	[°C]	[%]	[hPa]	[m]
sensor	*Kipp and Zonen CNR1*			*Young 05103*		CNR1	*Vaisala HMP45*		*Setra 278*	*SR50*
26/12 - 11/12	413	0.54	205	3.0	170	-5.3	-2.7	32.5	442	1.62
12/12 - 20/12	441	0.48	212	2.8	214	-2.9	-0.8	41.4	448	1.96
21/12 - 03/01	426	0.41	224	3.1	217	-1.4	1.9	39.5	456	2.56

Table 3: Surface roughness (z_0) computed according to Munro (1989) on detrended profiles longer than 1.5 m, extracted at 0.10 m intervals from the Kinect surface meshes at site A and B for E-W impinging wind and N-S impinging wind. The number of profiles used for each wind direction is given in parenthesis. The likely displacement of the zero velocity plane (d_top ± standard deviation), was computed as the mean of 2/3h for all profiles and expressed as a distance from the top of the penitentes. The range of the detrended 3D mesh (3D range) provides a reference for the penetration depth of turbulence.

	site A						**site B**					
	z_0 E-W (20)			**z_0 N-S (33)**			**z_0 E-W (6)**			**z_0 N-S (7)**		
	mean	**max**	**min**	**mean**	**max**	**min**	**mean**	**max**	**min**	**mean**	**max**	**min**
25-Nov	45	111	11	8	19	3						
11-Dec	33	68	12	6	13	2	28	41	22	6	9	1
20-Dec	70	146	57	25	67	7	122	156	84	22	47	14
03-Jan	136	211	71	45	136	11	133	186	101	21	30	12
	3D range [m]	**d_top +/- std [m]**		**3D range [m]**	**d_top +/- std [m]**		**3D range [m]**	**d_top +/- std [m]**		**3D range [m]**	**d_top +/- std [m]**	
25-Nov	0.41	0.27	0.06	0.41	0.34	0.02						
11-Dec	0.48	0.33	0.05	0.48	0.41	0.01	0.58	0.45	0.02	0.58	0.51	0.02
20-Dec	0.76	0.58	0.03	0.76	0.61	0.04	0.98	0.76	0.02	0.98	0.84	0.04
03-Jan	1.07	0.79	0.03	1.07	0.86	0.05	1.14	0.86	0.03	1.14	0.98	0.02

Figure 1: Map of Tapado Glacier in the Elqui catchment of the Coquimbo Region of Chile, showing the location of the measured sites and insets of (a) the glacier site layout, showing the location of the horizontal reference (black line) and (b) the test site, indicating the boulder (red star) at which the Kinect scans were compared against TLS

Figure 2: (a) Oblique view of the TLS-derived DSM of the test site highlights the patchy coverage of the penitentes obtained by this method. (b) Absolute differences between DSMs of the sample boulder produced using TLS and Kinect.

Figure 3: Shaded DSM meshes of N-S orientated DSMs for the 1.5 m x 1.5 m glacier site B on (a) 12.12.2013 (b) 20.12.2013 and (c) 03.01.2013 obtained using the Kinect.

Figure 4: Summary of the DSM properties through time at site A (left) and B (right). (a,b) Surface height distribution as a percentage of total surface area, in local coordinates [m] relative to the position of the northern end of ablation frame.Inset tables show weighted mean mesh elevation, range, surface area and surface area as a function of the horizontal area of the sampled site. (c,d) Distribution of surface angles as a percentage of total surface area. (e,f) Aspect distribution as a percentage of total surface area.

Figure 5: Comparison of surface height through time from manual measurements (points) and extracted from the Kinect scans (solid lines ± vertical error) along the horizontal reference (site A, Figure 1). Triangles indicate original snow depth compared to the surface measured on 25/11/13 and solid black triangles indicate locations where snowdepth exceeded the length of the 3 m probe

Figure 6: Representative surface heights computed on detrended surface meshes for site A (solid) and site B (open) over time where h1-h4 refer to representative surface heights computed as range (h1), twice the standard deviation (h2), area weighted mean height above the minimum (h3), and area weighted median above the minimum mesh height (h4).

Figure 7: 3D z_0 computed for 10° aspect intervals for all detrended DSMs highlighting peak roughness occurs in N-S airflow. Maximum values take *h* to be the detrended mesh elevation range, and minimum values take *h* to be twice the standard deviation of the detrended mesh.

Figure 8: Comparison of three-dimensional surface roughness through time, indicating the range of z_0 computed for all incident wind angles (at 10° intervals). Upper panels show the roughness with no zero level displacement and lower panels show values with a zero displacement offset $d1 = h$; $d2 = 2/3h$ and $d3 = 1/3h$. As before, *h1*- *h4* refer to representative surface heights computed as range, twice the standard deviation, area weighted mean height above the minimum, and area weighted median above the minimum mesh height respectively.

Figure 9: Examples of (a) N-S, and (b) E-W orientated cross sections longer than 1.5 m, sampled at 0.1 m intervals from which effective surface roughness properties were computed using the methods of Munro (1989, 1999).The local coordinates are relative to the NE corner marker of site A (Fig 1).

Figure 10: Wind rose for the whole study period (26 Nov 2013 – 3 Jan 2014).

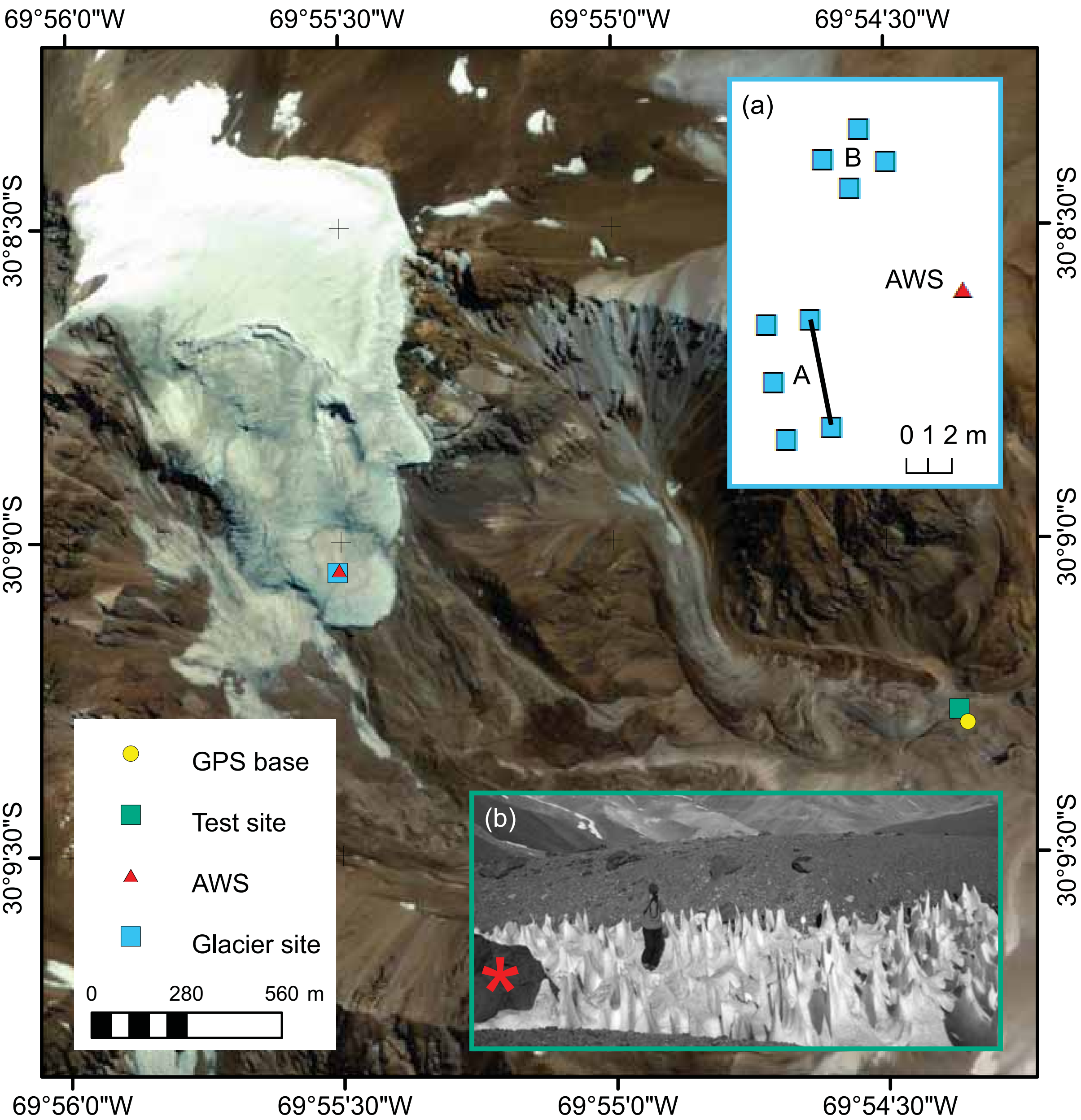
69°56'0"W
69°55'30"W
69°55'0"W
69°54'30"W
30°8'30"S
30°9'0"S
30°9'30"S
(a)
B
AWS
A
0 1 2 m
GPS base
Test site
AWS
Glacier site
0
280
560 m
(b)

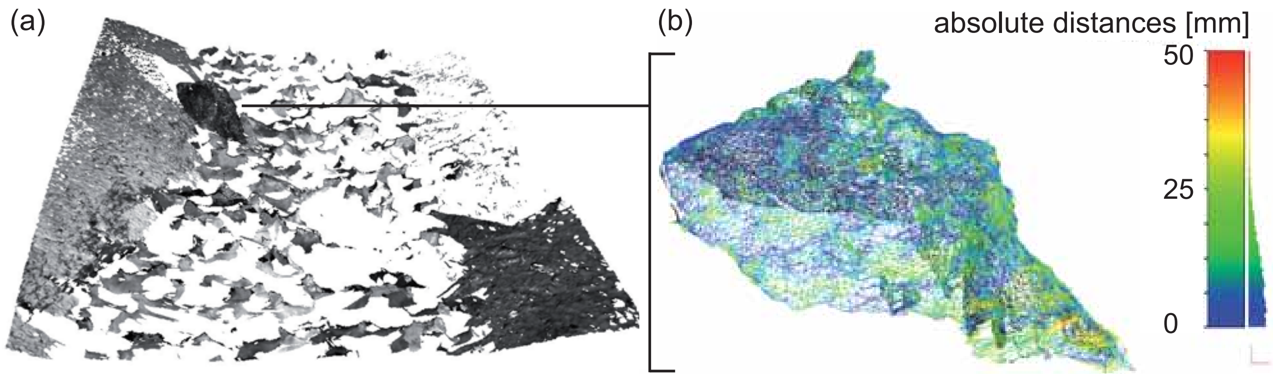

(a)
(b)
absolute distances [mm]
50
25
0

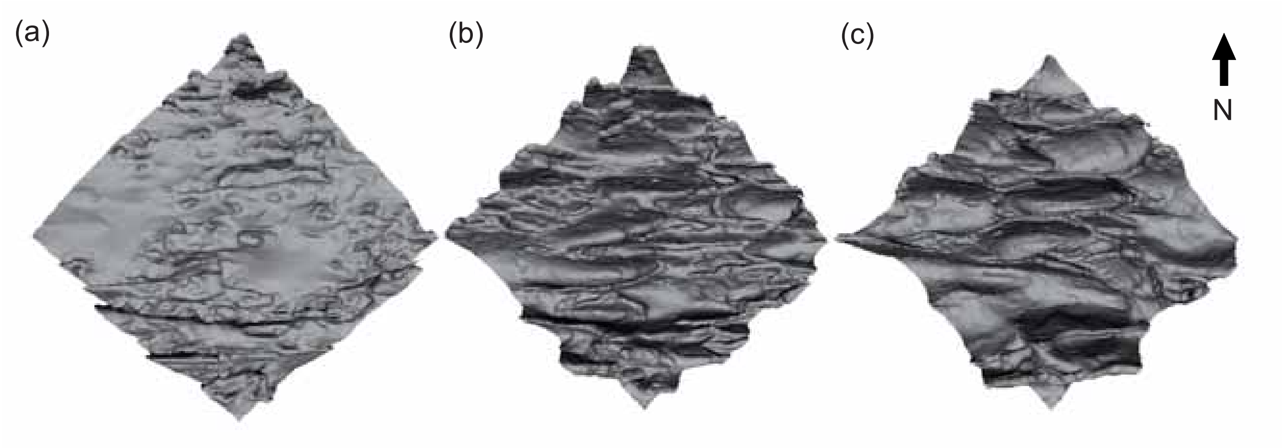

(a)
(b)
(c)
N

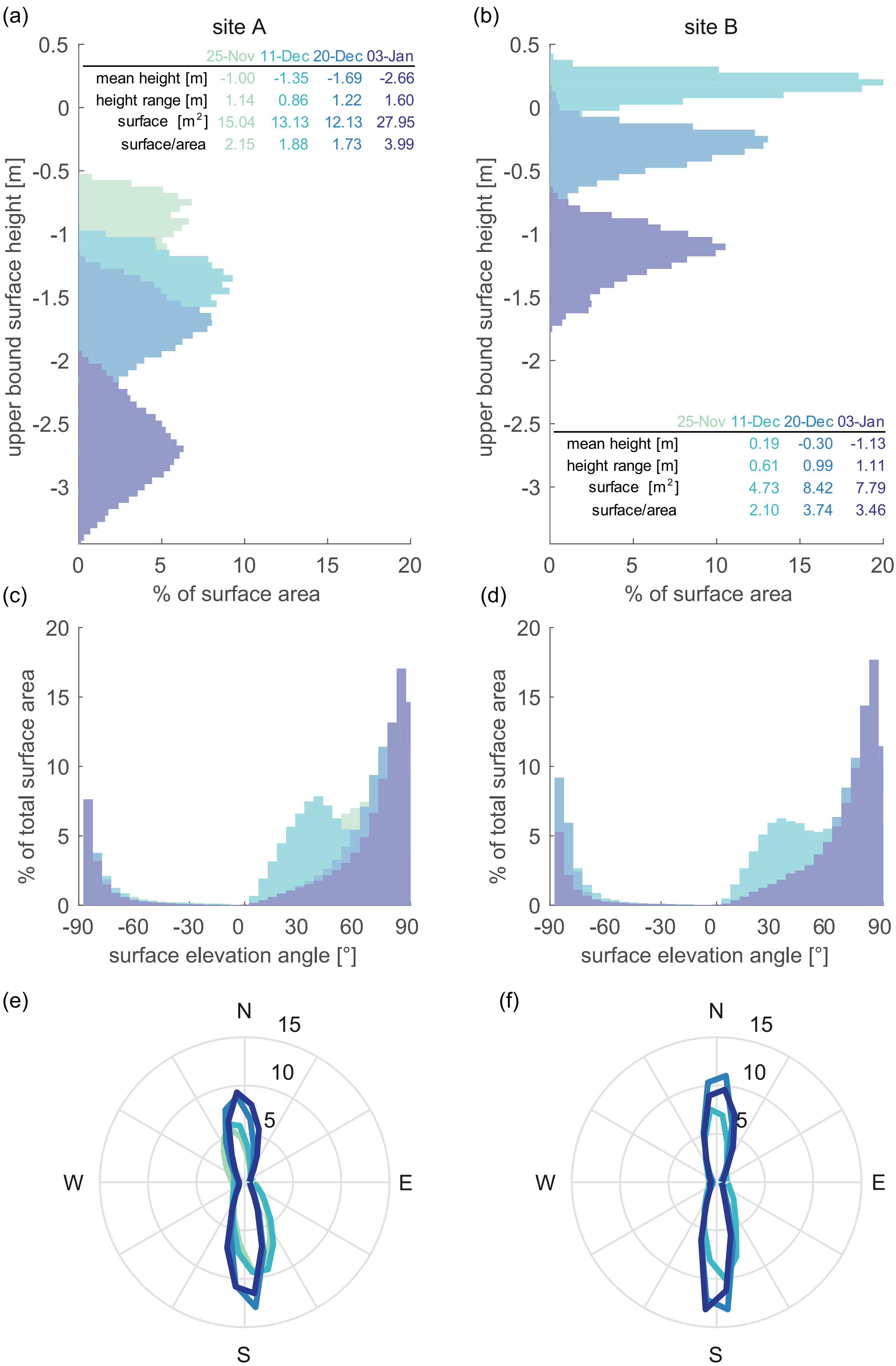

(a)
site A
25-Nov 11-Dec 20-Dec 03-Jan
mean height [m] -1.00 -1.35 -1.69 -2.66
height range [m] 1.14 0.86 1.22 1.60
surface [m^2] 15.04 13.13 12.13 27.95
surface/area 2.15 1.88 1.73 3.99
upper bound surface height [m]
% of surface area
(b)
site B
25-Nov 11-Dec 20-Dec 03-Jan
mean height [m] 0.19 -0.30 -1.13
height range [m] 0.61 0.99 1.11
surface [m^2] 4.73 8.42 7.79
surface/area 2.10 3.74 3.46
upper bound surface height [m]
% of surface area
(c)
% of total surface area
surface elevation angle [°]
(d)
% of total surface area
surface elevation angle [°]
(e)
N
E
S
W
(f)
N
E
S
W

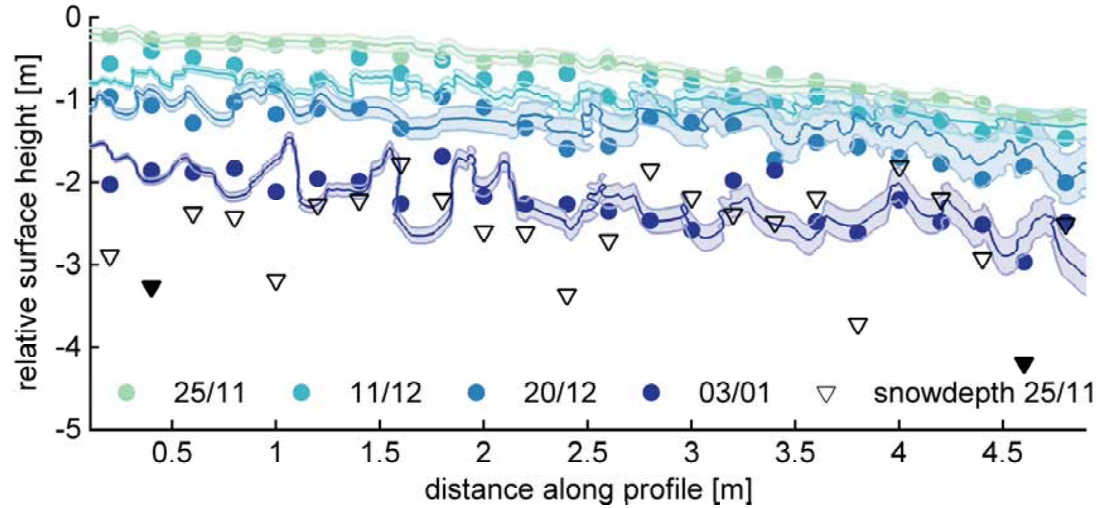

relative surface height [m]
0
-1
-2
-3
-4
-5
25/11
11/12
20/12
03/01
snowdepth 25/11
0.5
1
1.5
2
2.5
3
3.5
4
4.5
distance along profile [m]

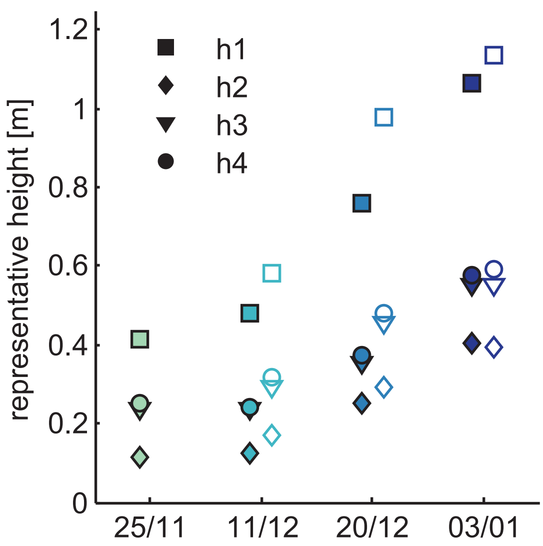

h1
h2
h3
h4
representative height [m]
1.2
1
0.8
0.6
0.4
0.2
0
25/11
11/12
20/12
03/01

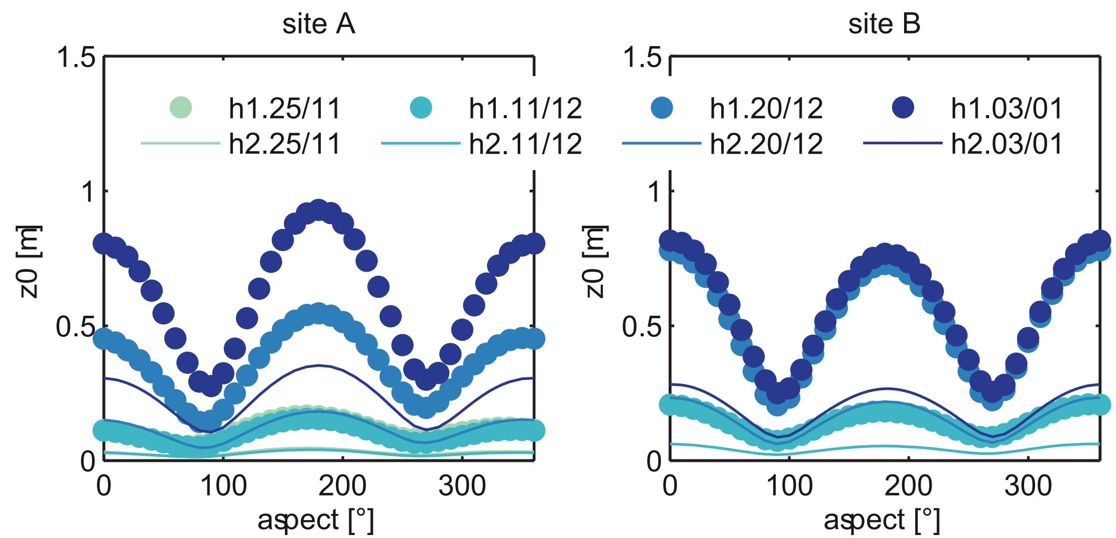
site A
site B
h1.25/11
h2.25/11
h1.11/12
h2.11/12
h1.20/12
h2.20/12
h1.03/01
h2.03/01
z0 [m]
aspect [°]
0
0.5
1
1.5
0
100
200
300

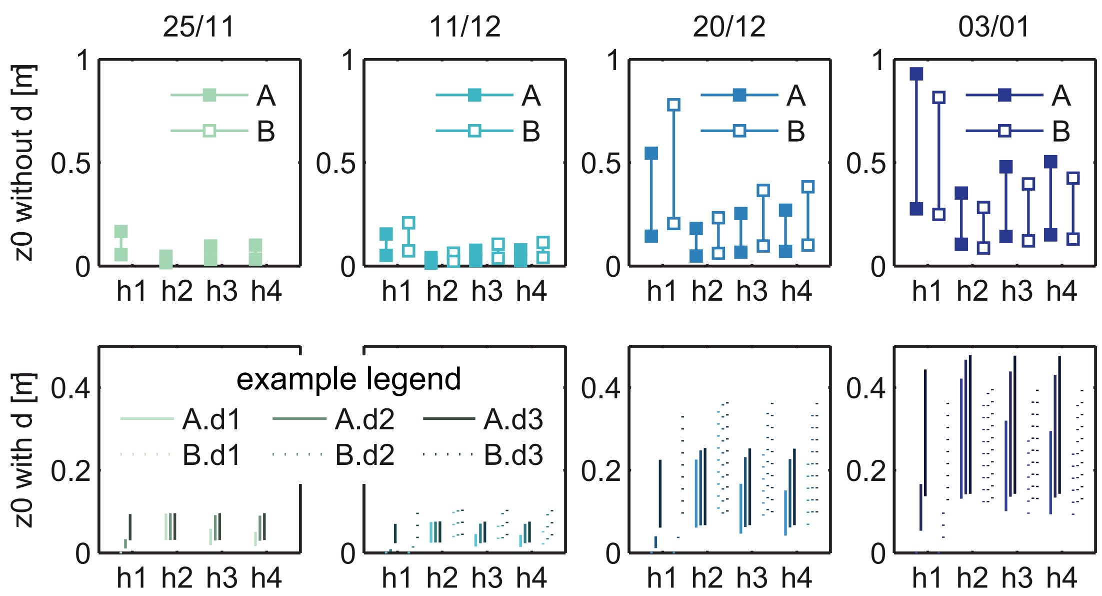

25/11
11/12
20/12
03/01
z0 without d [m]
z0 with d [m]
A
B
h1 h2 h3 h4
example legend
A.d1
A.d2
A.d3
B.d1
B.d2
B.d3

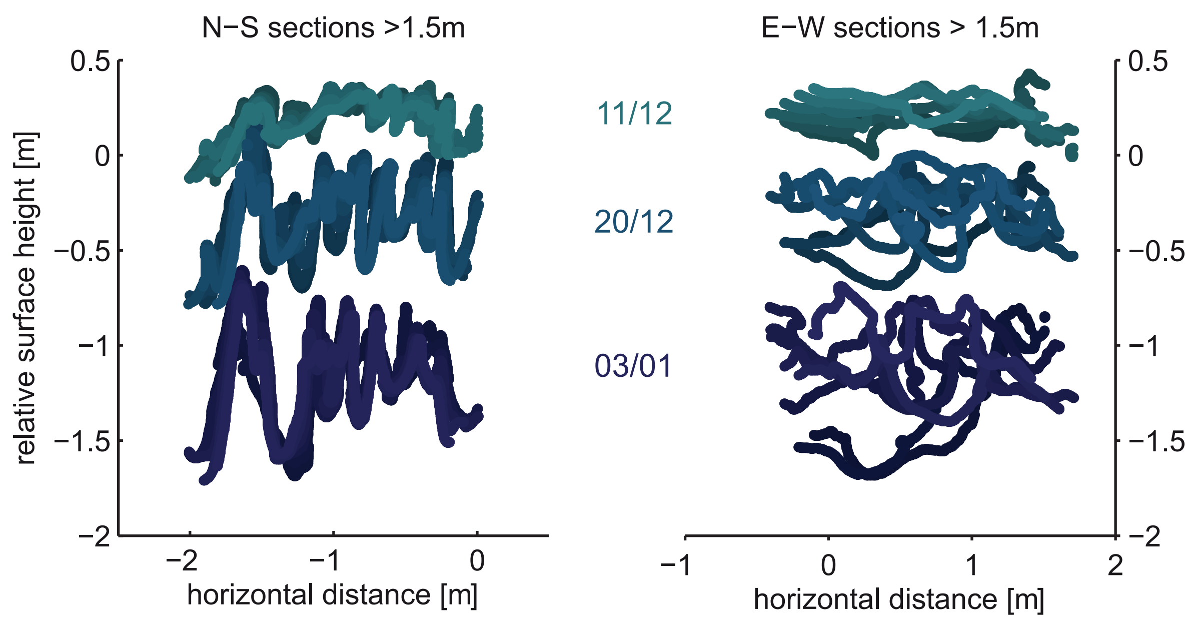
N−S sections >1.5m
E−W sections > 1.5m
relative surface height [m]
horizontal distance [m]
horizontal distance [m]
11/12
20/12
03/01
0.5
0
−0.5
−1
−1.5
−2
−2
−1
0
−1
0
1
2

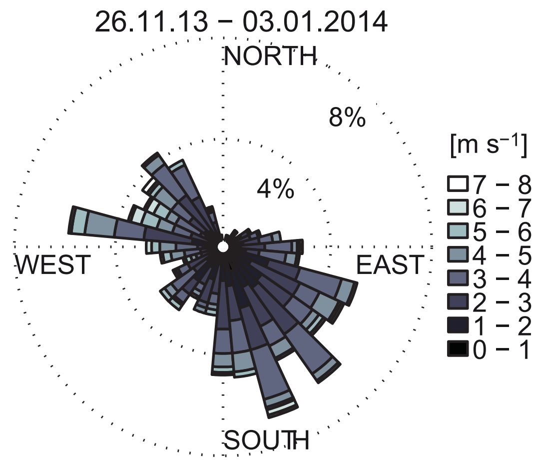
26.11.13 − 03.01.2014
NORTH
8%
4%
WEST
EAST
SOUTH
[m s⁻¹]
7 − 8
6 − 7
5 − 6
4 − 5
3 − 4
2 − 3
1 − 2
0 − 1